Available online at www.sciencedirect.com

SciVerse ScienceDirect

Ceramics International 39 (2013) 7595–7603

CERAMICS INTERNATIONAL

www.elsevier.com/locate/ceramint

Mechanical properties of zirconia composite ceramics

Y. Zhang[a,b,c,*], J. Malzbender[a], D.E. Mack[a], M.O. Jarligo[a], X. Cao[b], Q. Li[d], R. Vaßen[a], D. Stöver[a]

[a]Forschungszentrum jülich GmbH, IEK, 52425 Jülich, Germany

[b]State Key Laboratory of Rare Earth Resources Utilization, Changchun Institute of Applied Chemistry, Chinese Academy of Sciences, Changchun 130022, Jilin, China

[c]AVIC Harbin Dongan Engine (Group) Co., Ltd., Harbin 150066, China

[d]Harbin University of Science and Technology, College of Material Science & Engineering, Harbin 150040, China

Received 7 February 2013; received in revised form 12 February 2013; accepted 2 March 2013
Available online 14 March 2013

Abstract

Composite materials based on 8 wt% yttria partially stabilized zirconia, with additions of gadolinium zirconate, lanthanum lithium hexaaluminate, yttrium aluminum garnet and strontium zirconate were characterized. Samples were fabricated by hot-press sintering at 1550 °C. The effect of the secondary phase content on the mechanical properties of the composites was evaluated. Hardness, elastic modulus and fracture toughness of the fabricated composites were determined by means of depth-sensitive indentation testing. The fracture toughness of the samples as determined by the indentation method was found to increase with increasing YSZ content, reaching 3 MPa·$m^{0.5}$ for samples with 80 wt% YSZ. The fracture toughness appeared to be affected by thermal expansion coefficient mismatch, crack bridging and crack deflection.

Keywords: B. Composites; C. Mechanical properties; Toughness; Ceramics

1. Introduction

Mechanical properties play a crucial role in the long-term reliability of advanced ceramics and are therefore a critical factor for the operation of ceramics based components. In general, high fracture toughness and low elastic modulus value appear to be advantageous to reduce the crack growth under a discrete thermal stress levels. However, the often observed low toughness of some newly developed ceramics can lead to enhanced crack growth at low stress levels [1].

The mechanical properties of ceramics are strongly determined by their microstructure, in particular phase components and composition of grain boundary phases as well as residual stress and microcracks [2]. A variation of the parameters can lead to different microstructures, which in turn will have a strong impact on the rather macroscopically measured mechanical properties like hardness and stiffness. Although often used as porous materials or applied as a coating for example in the case of thermal barriers [3,4]; the properties of the ceramic still depend on the underlying basic properties of the material, which can be determined for dense specimens.

In general, a variety of approaches to improve the fracture toughness of ceramics exist, and toughening mechanisms include phase transformation, microcracking, nanofication, fiber/whisker reinforcement, and grain bridging [5]. The addition of the second phase has also been considered as an important improvement means by hindering crack propagation [6].

In the current work phase analysis, microstructure and mechanical properties of a series of ceramic materials based on 8 wt% yttria partially stabilized zirconia (YSZ), with additions of gadolinium zirconate ($Gd_2Zr_2O_7$), lanthanum lithium hexaaluminate ($LaLiAl_{11}O_{18.5}$), yttrium aluminum garnet ($Y_3Al_5O_{12}$) and strontium zirconate ($SrZrO_3$) are reported. Hot pressing is used to compact the ceramics to full density, which involves the simultaneous application of pressure and heat to the 'green' component [7].

*Corresponding author at: State Key Laboratory of Rare Earth Resources Utilization, Changchun Institute of Applied Chemistry, Chinese Academy of Sciences, Changchun 130022, Jilin, China. Tel./fax: +86 431 85262285.
E-mail address: yfzhang_2007@hotmail.com (Y. Zhang).

0272-8842/$ - see front matter © 2013 Elsevier Ltd and Techna Group S.r.l. All rights reserved.
http://dx.doi.org/10.1016/j.ceramint.2013.03.014

2. Experimental

Spray-dried powders of novel materials developed and produced in house were used as the starting materials. The additionally YSZ powders used in this study were 8 wt % YSZ (204B-NS HOSP™, Sulzer Metco, Westbury, NY, US) with an average particle size of 75±44 μm. Powder mixtures were ball-milled with ethanol for 24 h and then dried. The powder mixtures were cold-pressed under 30 kN into 10 mm diameter discs and then hot-pressed at 1550 °C for 2 h in vacuum, with an applied uniaxial load of 600 kgf using a graphite die (Fig. 1a).

The temperature program for hot-pressing is as follows: (a) heating from room temperature to 1200 °C with a rate of 15 K/min; (b) increase the temperature from 1200 °C to 1550 °C with a rate of 5 K/min; (c) keep the sintering temperature for the desired duration of 2 h; and (d) cool down from the sintering temperature to room temperature with a rate of 15 K/min. After hot-pressing, the discs were annealed at 1400 °C for 12 h in air to remove the surface graphite. Fig. 1b and c show hot-pressed sample before and after annealing, respectively.

The densities of the hot-pressed samples were measured using the Archimedes method. The disk-shaped samples were vacuum impregnated with epoxy. After resin hardening, the sample was ground mechanically with SiC abrasive paper, and polished with diamond suspension.

A Fischerscope H100C (Helmut Fischer GmbH, Sindelfingen, Germany) depth-sensitive indentation method was used to determine the hardness and elastic modulus [8–10] of the specimens following the procedure outline in DIN ISO 14577. The indenter was a standard Vickers diamond. Loads of 10 mN, 100 mN and 1000 mN loads were applied on the polished surface perpendicular to the hot-pressing axis. At the low loads of up to 1 N, it was not always possible to induce cracks for fracture toughness measurement using the depth sensitive indentation device. Hence, 10 N and 50 N indentations were carried out using a conventional hardness tester. The length of the indentation cracks was measured using the optical microscope of the Fischerscope indentation system (magnification of 20, 40 and 400). The calculation of the fracture toughness was based on the relationships given in [8,10].

Cracks paths at a higher magnification were also visualized with a scanning electron microscopy (SEM, Ultra 55, Zeiss, Oberkochen, Germany) that was equipped with an energy-dispersive X-ray analyzer (EDX, INCA, Oxford Instruments, Oxford, Great Britain). The X-ray diffraction (XRD) analyses of the samples were carried out with a D4 Endeavor diffractometer (Bruker AXS, Germany) operating with Cu Kα radiation source.

3. Results and discussions

3.1. XRD phase analysis and microstructure characterization

The XRD patterns of $SrZrO_3$ before and after hot-pressing are given in Fig. 2a–b. Hot-pressing improves the crystallization as shown by the higher peak intensity. The XRD patterns of YSZ–$SrZrO_3$ mixture after hot-pressing are displayed in Fig. 2c–e. The $SrZrO_3$ peaks intensity decreases as the YSZ fraction increases. The YSZ remains in tetragonal phase with only traces of monoclinic phase, indicating it remains stable after mixing with $SrZrO_3$. No other phases can be detected in the densified sample, implying that the hot-pressing process does not lead to a significant reaction between YSZ and $SrZrO_3$. Fig. 2f–g give the XRD patterns of YSZ

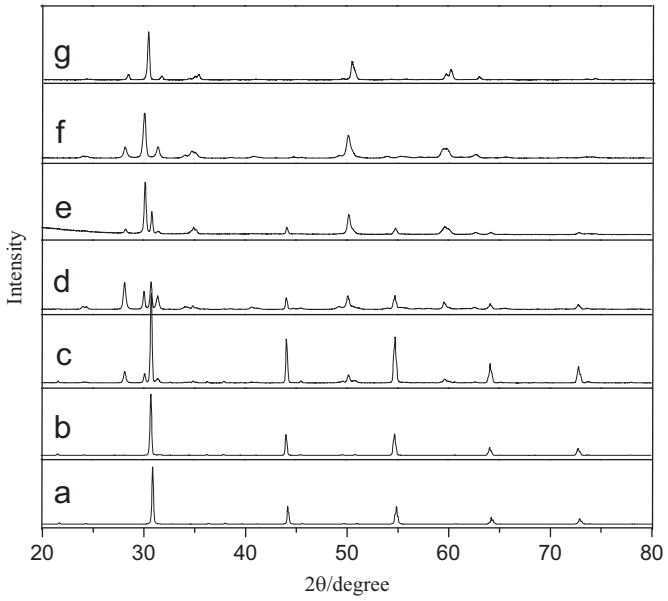

Fig. 2. XRD patterns of raw $SrZrO_3$ powders (a) and hot-pressed $SrZrO_3$ (b), 20 wt% YSZ+80 wt% $SrZrO_3$ (c), 50 wt% YSZ+50 wt% $SrZrO_3$ (d), 80 wt% YSZ+20 wt% $SrZrO_3$ (e), YSZ (f) and YSZ raw powders (g).

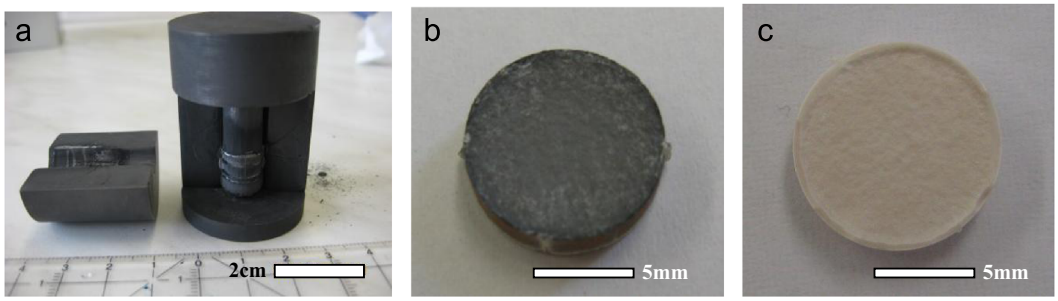

Fig. 1. (a) The graphite die used for hot-pressing; (b) sample after hot-pressing in vacuum and (c) hot-pressed sample after annealing.

before and after hot-pressing. The starting powder is mostly in the tetragonal phase with traces of monoclinic phase. No new phases were found after hot-pressing, indicating that also the YSZ remains stable during hot-pressing. That no reaction occurred between $SrZrO_3$ and YSZ is also verified by the EDX analysis (Fig. 3), verifying that the compositions of the gray and bright areas in the image are $SrZrO_3$ and ZrO_2, respectively.

The XRD patterns of the $LaLiAl_{11}O_{18.5}$ before and after hot-pressing are displayed in Fig. 4a–b. Before hot-pressing, $LaLiAl_{11}O_{18.5}$ crystallized in the hexagonal magnetoplumbite structure similarly to $LaMgAl_{11}O_{19}$. The phases $LaAlO_3$, $LiAl_5O_8$ and Al_2O_3 can already be detected in the powder. Hot-pressing leads to better crystallization of $LaLiAl_{11}O_{18.5}$ and only small amounts of $LaAlO_3$ can be detected (Fig. 4a). The initially observed $LiAl_5O_8$ and Al_2O_3 disappeared.

Fig. 4c–e illustrates the XRD patterns of YSZ–$LaLiAl_{11}O_{18.5}$ mixtures after hot-pressing. The phases ZrO_2 (*t*), ZrO_2 (*m*), $LaLiAl_{11}O_{18.5}$ and $LaAlO_3$ can be detected in the samples and no new phase is formed, verifying that no significant reaction occurs between YSZ and $LaLiAl_{11}O_{18.5}$. In addition, the increased peaks intensities in Fig. 4c and d indicate preferred crystal growth in the directions [0 1 2] and [−1 1 1] for $LaAlO_3$ and ZrO_2 (*m*), respectively. Again, the observations were confirmed with EDX. As shown in Fig. 5, grains of $LaLiAl_{11}O_{18.5}$ are homogeneously dispersed within the main YSZ matrix phase. Spectrum 1 presents the characteristic peaks assigned to the La, Al and O lines. The amount of these chemical elements corresponds to the chemical composition of $LaLiAl_{11}O_{18.5}$, however without Li. Spectrum 2 verifies that the composition of the bright area is ZrO_2.

The XRD patterns of the $Gd_2Zr_2O_7$ samples before and after hot-pressing are shown in Fig. 6a–b. $Gd_2Zr_2O_7$ was the only

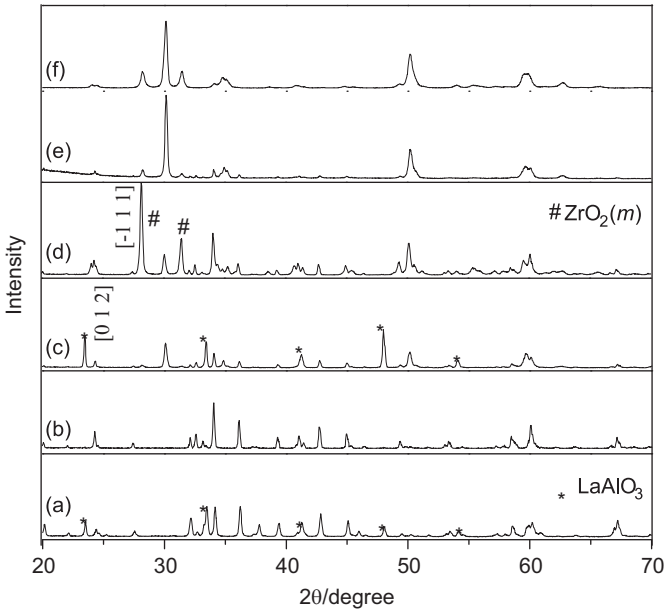

Fig. 4. XRD patterns of $LaLiAl_{11}O_{18.5}$ raw powders (a) and hot-pressed $LaLiAl_{11}O_{18.5}$ (b), 20 wt% YSZ+80 wt% $LaLiAl_{11}O_{18.5}$ (c), 50 wt% YSZ+50 wt% $LaLiAl_{11}O_{18.5}$ (d), 80 wt% YSZ+20 wt% $LaLiAl_{11}O_{18.5}$ (e), and YSZ (f).

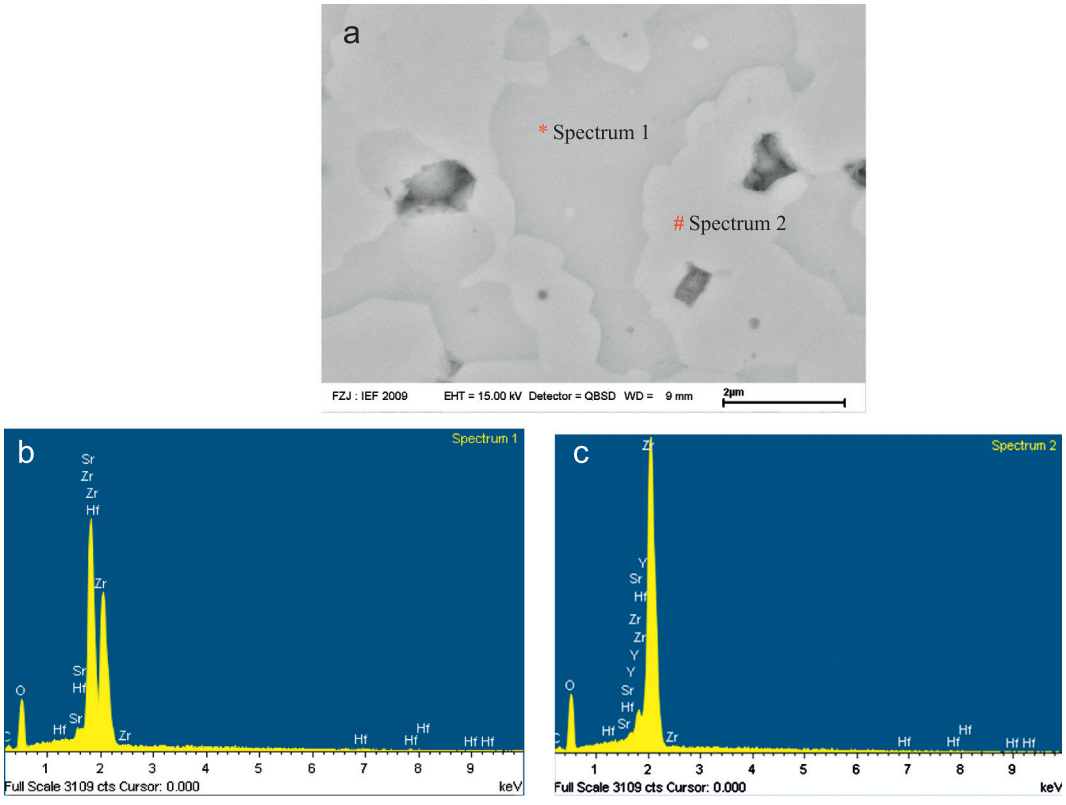

Fig. 3. SEM micrograph of polished surface of the YSZ–$SrZrO_3$ composite specimen and EDX displaying the composition of Spectrum 1and Spectrum 2.

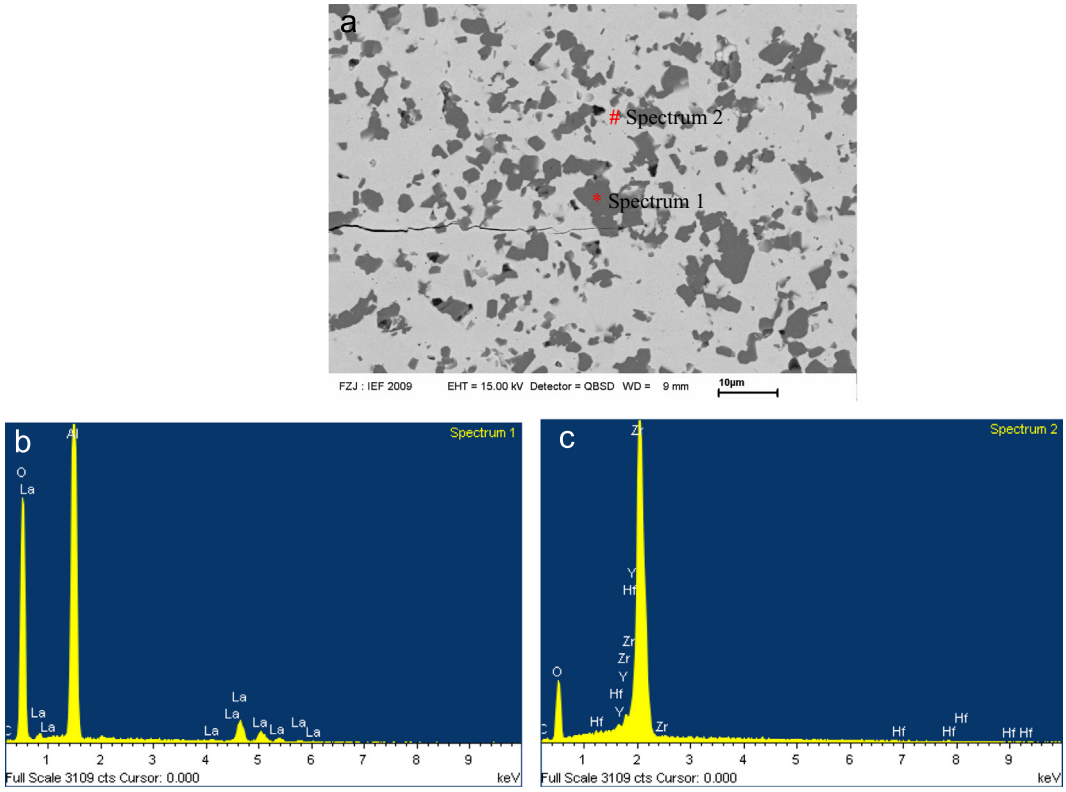

Fig. 5. SEM micrograph of a polished surface of the YSZ–$LaLiAl_{11}O_{18.5}$ composite specimen and an EDX analysis giving the composition of marked locations.

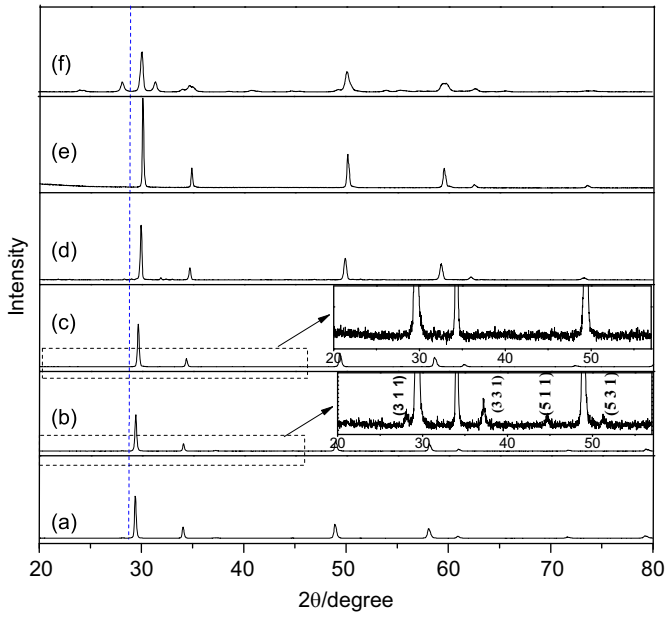

Fig. 6. XRD patterns of $Gd_2Zr_2O_7$ raw powders (a) and hot-pressed $Gd_2Zr_2O_7$ (b), 20 wt% YSZ+80 wt% $Gd_2Zr_2O_7$ (c), 50 wt% YSZ+50 wt% $Gd_2Zr_2O_7$ (d), 80 wt% YSZ+20 wt% $Gd_2Zr_2O_7$ (e), and YSZ (f). Insert shows superstructure diffraction peaks of pyrochlore-type structure.

phase detected in the powders. Hot-pressing leads to no additional new phases. $Gd_2Zr_2O_7$ has an ordered pyrochlore-type structure, which is characterized by the presence of typical superstructure diffraction peaks at the 2θ values of about 14° (1 1 1), 28° (3 1 1), 37° (3 3 1), 45° (5 1 1) and 51° (5 3 1) using Cu Kα radiation [11].

Complex oxides with the general formula $Ln_2Zr_2O_7$ (Ln = lanthanide) exhibit an ordered pyrochlore-type structure or a defective fluorite-type structure, which is mainly governed by the ionic radius ratio of $r(Ln^{3+})/r(Zr^{4+})$ [11]. The stability of the pyrochlore structure in zirconates at one atmospheric pressure is limited to the range of $1.46 \le r(Ln^{3+})/r(Zr^{4+}) \le 1.78$ [11]. The ionic radius of Zr^{4+} is 0.72 Å in the six-coordination; however, the ionic radius of Gd^{3+} is 1.053 Å in the eight coordination [11]. For $Gd_2Zr_2O_7$, the $r(Gd^{3+})/r(Zr^{4+})$ is equal to 1.46, which resides at the edge of the pyrochlore phase stability window [11].

The XRD patterns of YSZ–$Gd_2Zr_2O_7$ mixture after hot-pressing is presented in Fig. 6c–e. Hot-pressed pure $Gd_2Zr_2O_7$ has an ordered pyrochlore-type structure, while YSZ doped powders exhibit a defective fluorite-type structure. Replacing Gd in pyrochlore-type $Gd_2Zr_2O_7$ by smaller lanthanides Y ($R_{Gd} = 1.053 > R_Y = 1.019$ Å) will decrease the value of $r(Ln^{3+})/r(Zr^{4+})$ and induces a pyrochlore-to-fluorite phase transition [12,13]. Peaks shift toward higher angles and the peaks intensities increase when more YSZ is incorporated, indicating a decrease of the lattice parameters and the formation of the ZrO_2–Gd_2O_3 solid solutions when the Gd is replaced by the smaller Y. If YSZ is doped with $SrZrO_3$ or $LaLiAl_{11}O_{18.5}$, monoclinic and tetragonal ZrO_2 can be detected in the mixture. In YSZ–$Gd_2Zr_2O_7$ only cubic ZrO_2 can be detected, which might be due to stabilization by gadolinia. Additional EDX analysis also proves a reaction between YSZ and $Gd_2Zr_2O_7$. As shown in Fig. 7, the phase distribution of the polished surface is almost

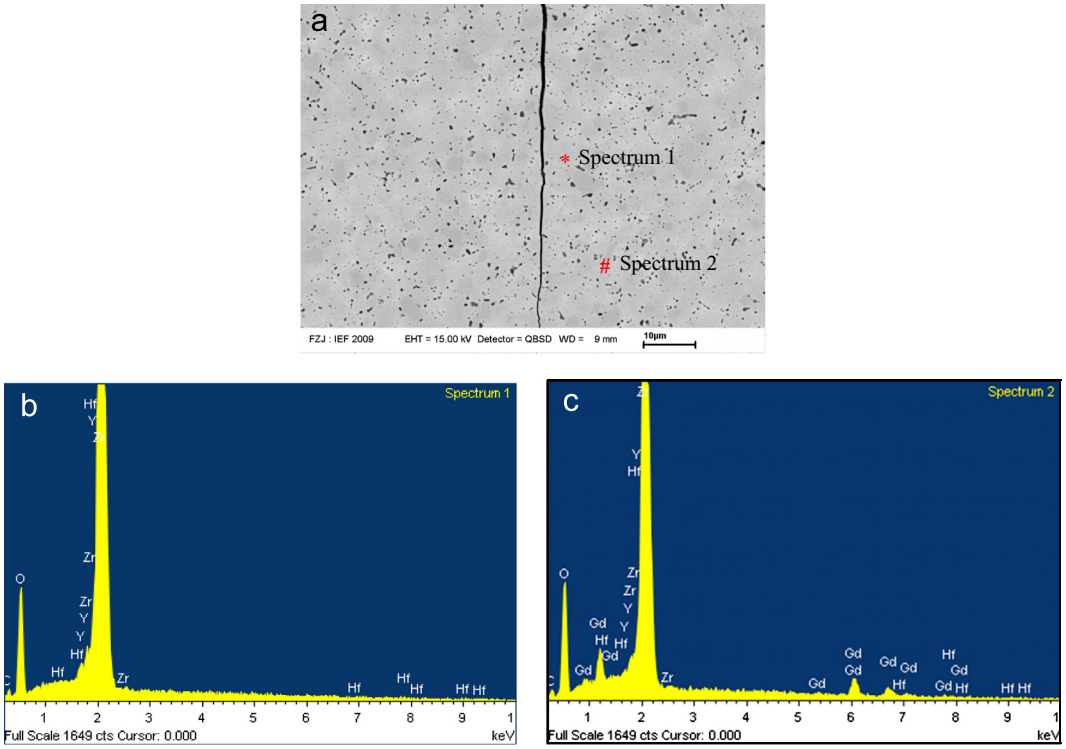

Fig. 7. SEM micrograph of polished surface of the YSZ–$Gd_2Zr_2O_7$ composite and EDX analysis giving the composition of Spectrum 1 and Spectrum 2.

homogenous. The EDX results indicate that the composition of gray area is ZrO_2 (Spectrum 1). However, composition of the light area is $Gd_2Zr_2O_7$ with Y (Spectrum 2), which verifies the formation of ZrO_2–Gd_2O_3 solid solutions when the Gd is replaced by the smaller Y.

The XRD patterns of $Y_3Al_5O_{12}$ before and after hot-pressing are visualized in Fig. 8a–b. The main composition is $Y_3Al_5O_{12}$ (cubic garnet structure) and the secondary phase is a perovskite phase $YAlO_3$ (YAP, orthorombic structure). By solid-state reaction, high temperatures are required to prepare pure YAG or other yttrium aluminates. In fact, when the reactants are heated to a temperature below 1600 °C, a single-phase could not be obtained; $YAlO_3$ or Al_2O_3 are found.

Fig. 8c–e displays the XRD patterns of YSZ–$Y_3Al_5O_{12}$ mixture after hot-pressing. It can be seen that the crystalline phases in mixture are yttrium aluminum garnet ($Y_3Al_5O_{12}$, YAG), ZrO_2 (cubic) and corundum (α-Al_2O_3). No other phases were found and the initial $YAlO_3$ in the YAG sample disappeared. The Y of the $YAlO_3$ lattice might be dissolved in zirconia and the remaining Al precipitate as Al_2O_3. The Al_2O_3 peak intensities increase as more YSZ powders are incorporated. The initial ZrO_2 (*t*) and ZrO_2 (*m*) transform into ZrO_2 (*c*), which indicates a reaction between YSZ and $Y_3Al_5O_{12}$. The composition of the grains obtained from EDX analysis agrees with that obtained using XRD. Local spot EDX analysis has been carried out for four different regions. As shown in Fig. 9, the EDX analysis indicates that the compositions of bright (Spectrum 2) and gray (Spectrum 1) areas are YSZ and $Y_3Al_5O_{12}$, respectively. Spectrum 3 obtained at the interface has very intense $Y_3Al_5O_{12}$ peaks and smaller YSZ peaks, which indicates diffusion and reaction between YSZ and YAG. The dark

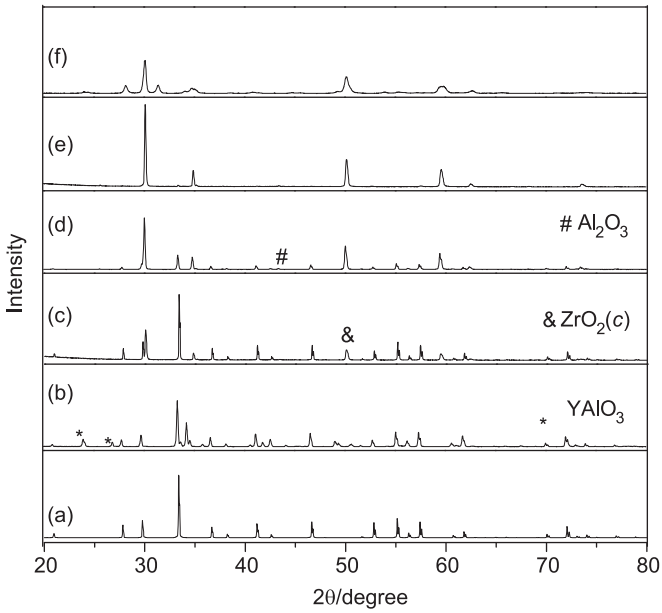

Fig. 8. XRD patterns of $Y_3Al_5O_{12}$ raw powders (a) and hot-pressed $Y_3Al_5O_{12}$ (b), 20 wt% YSZ+80 wt% $Y_3Al_5O_{12}$ (c), 50 wt% YSZ+50 wt% $Y_3Al_5O_{12}$ (d), 80 wt % YSZ+20 wt% $Y_3Al_5O_{12}$ (e), and YSZ (f).

area consists only of Al_2O_3 (Spectrum 4), which also indicates that Y from the $YAlO_3$ lattice has been dissolved in zirconia and the remaining Al precipitates as Al_2O_3.

3.2. Densification

The relative densities of the investigated materials are summarized in Fig. 10. All hot-pressed samples have relative

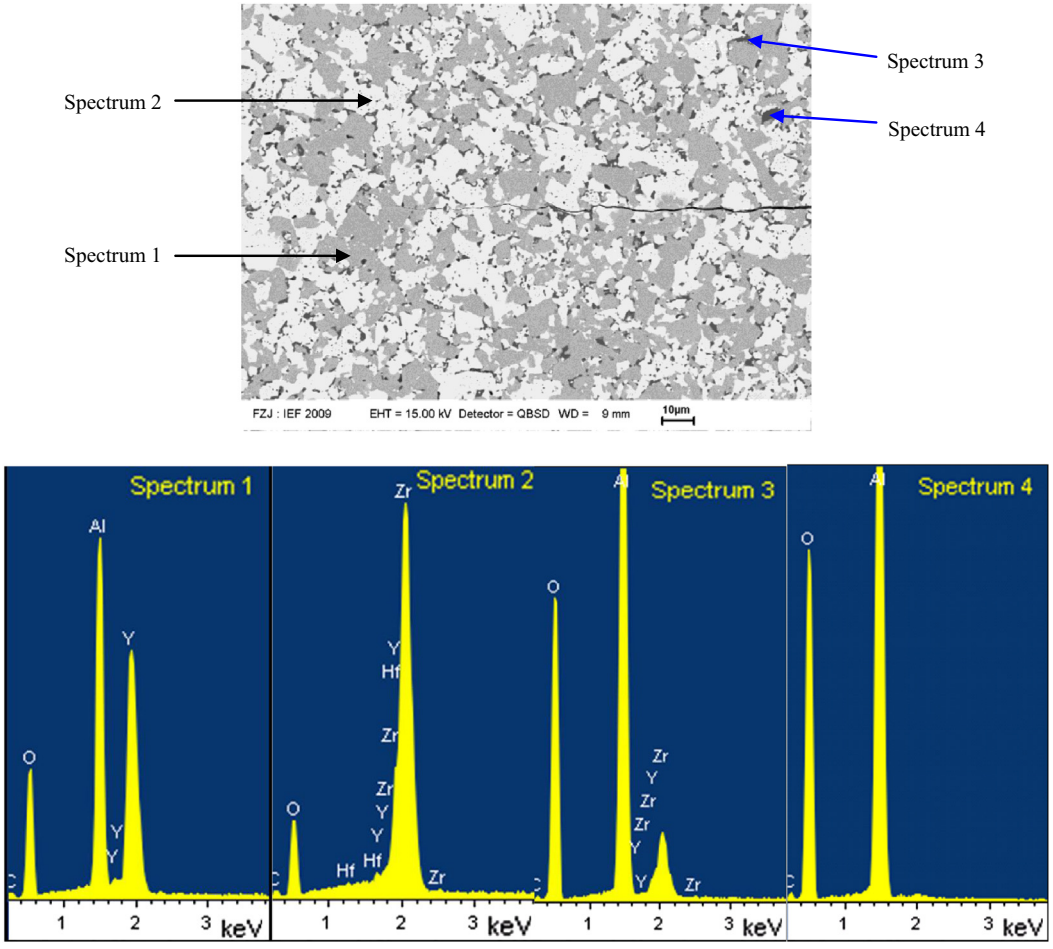

Fig. 9. SEM micrograph of polished surface of the YSZ–$Y_3Al_5O_{12}$ composite and the corresponding EDX analysis of different regions.

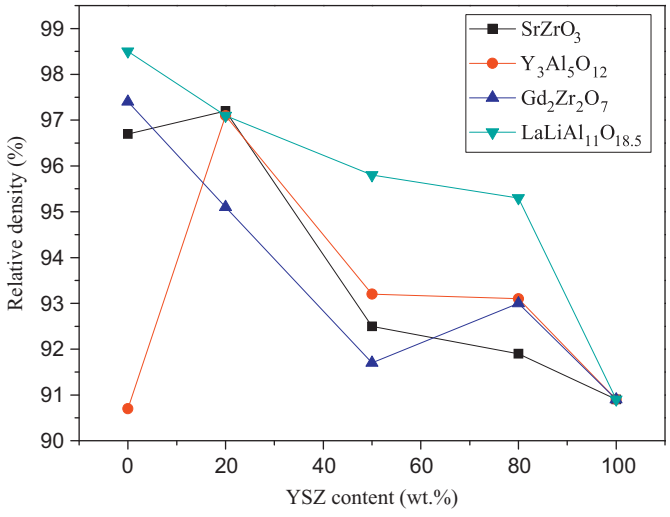

Fig. 10. Relative densities of the hot-pressed samples.

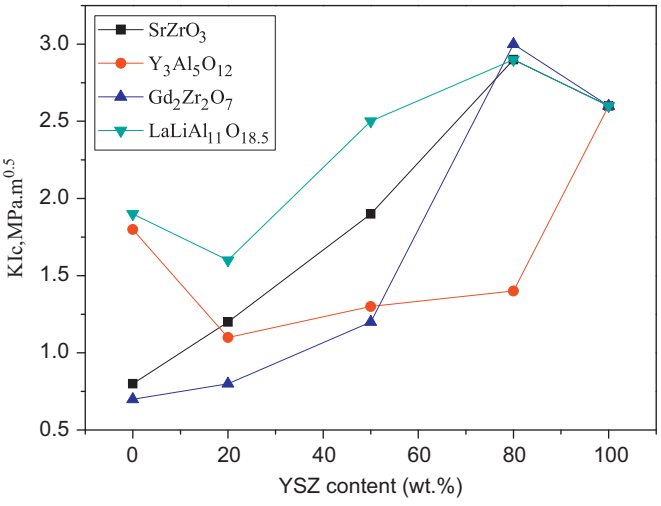

Fig. 11. Fracture toughness of the hot-pressed samples.

densities of more than 90%. The relative density increases with increasing secondary phase content. This result suggests that the addition of secondary phase can reduce the sintering temperature. The rather low values for YSZ prove that it is more sintering-resistant than the other materials (has a higher melting point and sintering temperature than the secondary phases) and the sintering temperature of YSZ composites can be reduced effectively by the addition of a secondary phase. Addition of secondary phases with low melting point lowers the liquid phase formation temperature and increases the liquid content, which aids sintering.

3.3. Mechanical properties

The indentation fracture toughness values are summarized in Fig. 11. The fracture toughness of the materials increases significantly with the amount of YSZ phase. The fracture toughness reaches 3.0 MPa·m$^{0.5}$ for the composite ceramics with 80 wt% YSZ. The fracture toughness of the pure YSZ appears to be slightly lower than expected, which might be a result of incomplete sintering that is also reflected in the rather low absolute density. Young's moduli decrease with increasing YSZ content (Fig. 12), which is advantageous with respect to thermal stresses. For most of the samples this is also reflected in the hardness (Fig. 13).

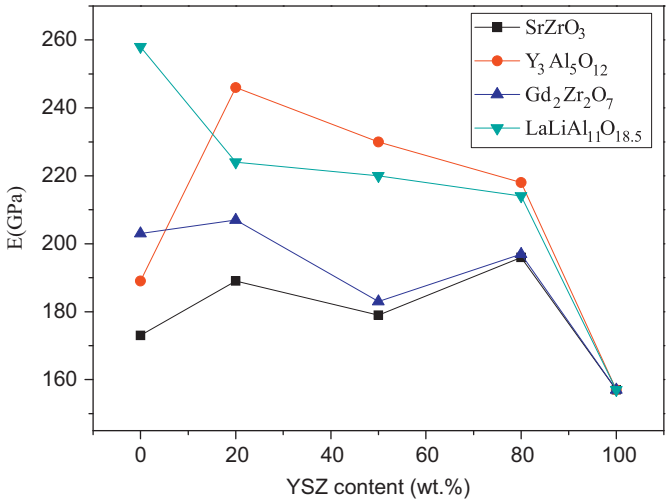

Fig.12. Young's modulus of the hot-pressed samples.

The fracture toughness improvement can be attributed to a combination of several toughening mechanisms, by grain sizes, TEC mismatch of the different phases, chemical reactions between the YSZ and the secondary phases. In order to clarify the mechanism, the crack morphology after indentation has been analyzed using an optical microscope. A typical indentation imprints after an indentation load with a load of 50 N is shown in Fig. 14a. Radial cracks are observed at all four corners of Vickers indentation. The fracture toughness for hot-pressed $SrZrO_3$ (Fig. 14a), is only 0.8 MPa·m$^{0.5}$. Parallel to the corner edge of the indenter, multiple cracks from single indent corner are observed. Around the indents, severe spallation is observed for this sample and part of the surface uplifts due to lateral crack growth.

The fracture toughness for hot-pressed 50 wt% YSZ+50 wt % $SrZrO_3$ (Fig. 14b) is 2.9 MPa·m$^{0.5}$, which is higher than that of pure YSZ and $SrZrO_3$. No indications of multiple cracking or uplift can be deserved. Only zigzag deflection (both tilting

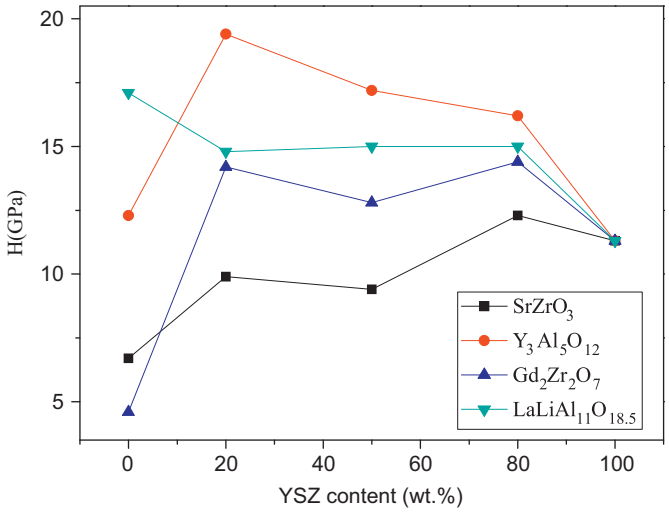

Fig. 13. Hardness of the hot-pressed samples.

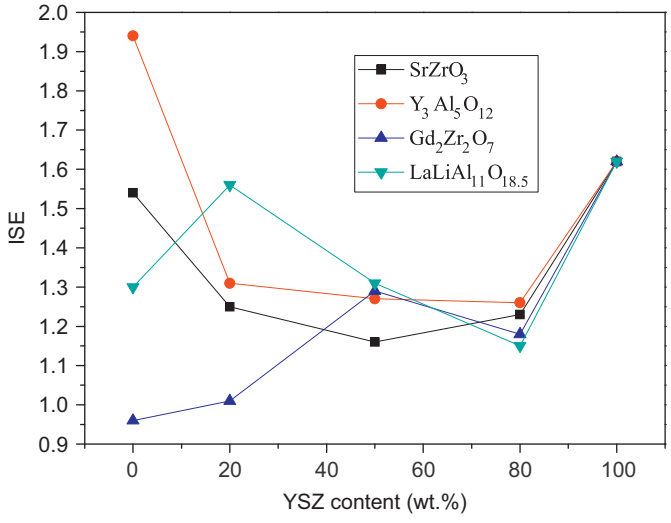

Fig. 15. ISE of hot-pressed samples.

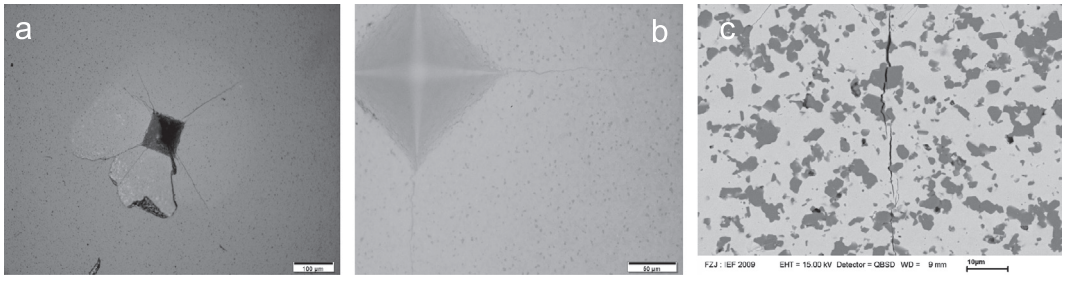

Fig. 14. Optical micrograph of indentation imprints on hot-pressed $SrZrO_3$ (a) and 50 wt%YSZ+50 wt% $SrZrO_3$ (b); SEM image of the hot-pressed 80 wt% YSZ+20 wt% $LaLiAl_{11}O_{18.5}$ after micro-indentation (c).

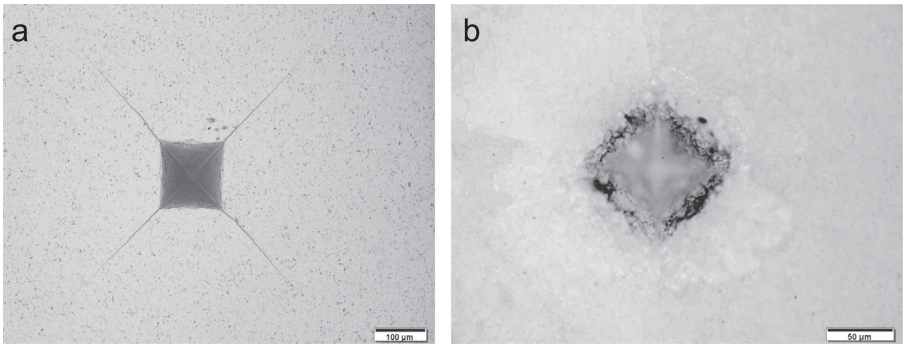

Fig. 16. Optical micrograph of indentation imprints on hot-pressed 80 wt% YSZ+20 wt% $Gd_2Zr_2O_7$ (a) and $Y_3Al_5O_{12}$ (b).

and twisting) can be observed. A crack which encounters either fracture-resistant second-phase particles or localized residual stress fields can be deflected out of the plane normal to the applied tensile stress [14]. One major cause for the crack deflection and toughening appears to be the difference in thermal expansion coefficient between the secondary phases and the YSZ. Thermal expansion mismatch stresses can cause crack tilting and twisting. The thermal expansion coefficient of YSZ is much higher than that of the secondary phases. This difference results in a compressive stress field and aids the crack deflection leading to an improvement of the interfacial strength between the secondary phases and the YSZ [15]. The presence of zigzag crack deflection consumes more fracture energy for separation, macroscopically manifested as increase in the apparent toughness.

In Fig. 14c an SEM image of the hot-pressed 80 wt% YSZ+20 wt% $LaLiAl_{11}O_{18.5}$ after micro-indentation is presented. The fracture toughness determined for this material is 2.9 MPa $m^{0.5}$. For hexaaluminates-containing samples, platelets can promote crack deflection and crack bridging. It has been reported that in the case of intergranular crack growth aluminate platelets like $LaAl_{11}O_{18}$, $LaMgAl_{11}O_{19}$, $SrAl_{12}O_{19}$ and $Mg_2NaAl_{15}O_{25}$ can improve the fracture toughness due to the anisotropy of the elongated grains [16]. The fracture mode is mostly trans-granular. Only a few areas of inter-granular cracks can be observed in the case of fine grains. Secondary-phase chemistry plays a dominant role in controlling the interfacial bonding, which in turn determines whether the crack advances in a transgranular or an intergranular mode [17]. The occurrence of both transgranular and intergranular crack propagation might be an indication of a non-uniform distribution of secondary phases at grain boundaries. Weaker grain boundaries lead to intergranular fracture and stronger grain boundaries to transgranular fracture which then increases the apparent fracture toughness.

The measured hardness decreased with increasing load, an effect generally known as indentation size effect (ISE, here defined as the ratio of the hardness at 10 mN to the value at 1 N). An ISE has been observed for all specimens (Fig. 15). Reasons for ISE effects are discussed in [18]. A comparison of the hardness values with the respective indentation marks revealed that the load dependency is partly related to the formation of indentation cracks. For materials with small ISE values (hot-pressed 80 wt% YSZ+20 wt% $Gd_2Zr_2O_7$, ISE=1.18) the indents display well-developed sharp cracks extending from the corners of the impression (Fig. 16a). However, when the material has a large ISE value (hot-pressed $Y_3Al_5O_{12}$, ISE=1.94) delamination occurred and sometimes crack opening is small or cracks are hardly visible (Fig. 16b), the micro-damage is confined to the immediate vicinity of the indentation.

4. Conclusions

Most of the prepared materials remain stable during hot-pressing. Hot-pressed samples have a high relative density of more than 90%. In particular no unwanted reactions take place when YSZ is mixed with $SrZrO_3$ or $LaLiAl_{11}O_{18.5}$. Reactions takes place when YSZ is mixed with $Gd_2Zr_2O_7$ or $Y_3Al_5O_{12}$, which is confirmed by phase transformation from ZrO_2 (*t*) and ZrO_2 (*m*) to ZrO_2 (*c*). Hot-pressed pure $Gd_2Zr_2O_7$ has an ordered pyrochlore-type structure while YSZ doped powders exhibit a defective fluorite-type structure.

The fracture toughness of these samples are in the range of 0.8–3.0 MPa $m^{0.5}$. The fracture toughness of the samples determined by the indentation method was found to increase with increasing YSZ content, reaching values of about 3 MPa $m^{0.5}$ for the samples with 80 wt% YSZ. The inclusion of secondary phases into the YSZ effectively enhanced fracture toughness of YSZ. Multiple cracking and even severe delamination and spalling occur when the fracture toughness is low (0.8–1.2 MPa $m^{0.5}$). Samples with the highest fracture toughness values show indications of crack bridging and zigzag deflection. The dominant toughening mechanisms appear to be mainly crack deflection due to thermal expansion mismatch and the stronger interfacial bonding between secondary phases and YSZ.

Acknowledgments

The authors would like to thank Ms. M.Andreas for spray-drying of the powders, Mr. B. Coenen for hot-pressing of the samples, Mr. M. Kappertz and Dr. D. Sebold for the sample microstructure characterizations, Dr. W. Fischer and Mr. M. Ziegner for XRD measurements. The experiments described in this paper were carried out in Forschungszentrum Jülich GmbH and the first author was financially supported by NSFC-50825204 and CAS-DAAD program.

References

[1] R. Vaßen, N. Czech, W. Malléner, W. Stamm, D. Stöver, Influence of impurity content and porosity of plasma-sprayed yttria-stabilized zirconia layers on the sintering behavior, Surface and Coatings Technology 141 (2001) 135.

[2] Z. Zhang, L. Teng, W. Li, Mechanical properties and microstructures of hot-pressed MgAlON–BN composites, Journal of the European Ceramics Society 27 (2007) 319.

[3] W. Ma, D. Mack, J. Malzbender, R. Vassen, D. Stoever, Yb_2O_3 and Gd_2O_3 doped strontium zirconate for thermal barrier coatings, Journal of the European Ceramics Society 28 (2008) 3071.

[4] T. Wakui, J. Malzbender, R.W. Steinbrech, Strain dependent stiffness of plasma sprayed thermal barrier coatings, Surface and Coatings Technology 200 (2006) 4995.

[5] J. Li, H. Dai, X. Zhong, Y. Zhang, X. Ma, J. Meng, X. Cao, Lanthanum zirconate ceramic toughened by $BaTiO_3$ secondary phase, Journal of Alloys and Compounds 452 (2008) 406.

[6] J. Li, H. Dai, X. Zhong, Y. Zhang, X. Ma, J. Meng, X. Cao, Effect of the addition of YAG ($Y_3Al_5O_{12}$) nanopowder on the mechanical properties of lanthanum zirconate, Materails Science and Engineering: A 460-461 (2007) 504.

[7] V. Viswanathan, T. Laha, K. Balani, A. Agarwal, S. Seal, Challenges and advances in nanocomposite processing techniques, Materials Science and Enginerring: R 54 (2006) 121.

[8] J. Malzbender, G. de With, Scratch testing of hybrid coatings on float glass, Surface and Coatings Technology 135 (2001) 202.

[9] J. Malzbender, G. de With, A model to determine the interfacial fracture toughness for chipped coatings, Surface and Coatings Technology 154 (2002) 21.

[10] J. Malzbender, R.W. Steinbrech, Fracture test of thin sheet electrolytes for solid oxide fuel cells, Journal of the European Ceramics Society 27 (2007) 2597.

[11] Z. Liu, J. Ouyang, Y. Zhou, X. Xia, Effect of Sm substitution for Gd on the electrical conductivity of fluorite-type $Gd_2Zr_2O_7$, Journal of Power Sources 185 (2008) 876.

[12] J. Díaz-Guilléna, A. Fuentes, M. Díaz-Guillén, J. Almanza, J. Santamaría, C. León, The effect of homovalent A-site substitutions on the ionic conductivity of pyrochlore-type $Gd_2Zr_2O_7$, Journal of Power Sources 186 (2009) 349.

[13] F. Elfallagh, B. Inkson, Evolution of residual stress and crack morphologies during 3D FIB tomographic analysis of alumina, Journal of Microscopy 230 (2008) 240.

[14] R. Sarno, M. Tomozawa, Toughening mechanisms for a zirconia–lithium aluminosilicate glass–ceramic, Journal of Materials Science 30 (1995) 4380.

[15] J. Selsing, Internal Stresses in Ceramics, Journal of the American Ceramics Society 44 (1961) 419.

[16] X. Liu, X. Chen, Effects of $Sr_2Nb_2O_7$ additive on microstructure and mechanical properties of 3Y–TZP/Al_2O_3 ceramics, Ceramics International 28 (2002) 209.

[17] H. Kleebe, G. Pezzotti, G. Ziegler, Microstructure and fracture toughness of Si_3N_4 ceramics: Combined roles of grain morphology and secondary phase chemistry, Journal of the American Ceramics Society 82 (1999) 1857.

[18] N. Gao, Y. Miyamoto, D. Zhang, Dense Ti_3SiC_2 prepared by reactive HIP, Journal of Materials Science 34 (1999) 4385.